COMPARISON OF RANS AND DES MODELING AGAINST MEASUREMENTS OF LEADING EDGE FILM COOLING ON A FIRST-STAGE VANE

S. Ravelli*, G. Barigozzi

Department of Engineering and Applied Sciences, University of Bergamo
Marconi St. 5, 24044 Dalmine (BG), ITALY
silvia.ravelli@unibg.it; giovanna.barigozzi@unibg.it

ABSTRACT

The performance of a showerhead arrangement of film cooling in the leading edge region of a first stage nozzle guide vane was experimentally and numerically evaluated. A six-vane linear cascade was tested at an isentropic exit Mach number of Ma_{2s} = 0.42, with a high inlet turbulence intensity level of 9%. The showerhead cooling scheme consists of four staggered rows of cylindrical holes evenly distributed around the stagnation line, angled at 45° towards the tip. The blowing ratios tested are *BR* = 2.0, 3.0 and 4.0. Adiabatic film cooling effectiveness distributions on the vane surface around the leading edge region were measured by means of Thermochromic Liquid Crystals technique. Since the experimental contours of adiabatic effectiveness showed that there is no periodicity across the span, the CFD calculations were conducted by simulating the whole vane. Within the RANS framework, the very widely used Realizable k-ε (Rke) and the Shear Stress Transport k-ω (SST) turbulence models were chosen for simulating the effect of the *BR* on the surface distribution of adiabatic effectiveness. The turbulence model which provided the most accurate steady prediction, i.e. Rke, was selected for running Detached Eddy Simulation at the intermediate value of *BR* = 3. Fluctuations of the local temperature were computed by DES, due to the vortex structures within the shear layers between the main flow and the coolant jets. Moreover, mixing was enhanced both in the wall-normal and spanwise direction, compared to RANS modeling. DES roughly halved the prediction error of laterally averaged film cooling effectiveness on the suction side of the leading edge. However, neither DES nor RANS provided the expected

decay of effectiveness progressing downstream along the pressure side, with 15% overestimation of η_{av} at s/C =0.2.

INTRODUCTION

Heat loads are the largest along the leading edge of a first-stage stator vane. In particular, the highest temperature generally occurs at the leading edge where the stagnation point is located. Complex designs have been proposed to provide the most effective cooling for this crucial region while using the minimum amount of cooling air [1]. Typical airfoil design includes blunt leading edges to minimize heat transfer at the stagnation point, together with showerhead arrangement [2]. Showerhead generally consists of four to eight rows of holes for vanes and three to five rows of holes for blades. Holes are typically aligned radially, i.e. normal to the mainstream direction, with injection angles relative to the surface ranging from 20º to 45º [3].

In practice the leading edge film cooling has been a research topic over the last 30 years. Accordingly, there are several experimental studies in the open literature which have been conducted over simulated surfaces including flat plates, cylinders [4, 5] and also cylinders with flat afterbodies [6, 7].

Many studies have addressed the detail of the film cooling performance within the showerhead region. Most of them made use of the infrared thermography to provide high-resolution surface temperature distributions. It emerged that increasing the *BR* up to the tested value of 2.9 resulted in increased lateral average adiabatic effectiveness level at low and high turbulence, due to a shallow injection angle of 25° [8, 9]. Conversely, Nasir et al. [10] reported that an increase in *BR* from 1.5 to 2.5 has an adverse effect on the adiabatic effectiveness on the pressure side and has negligible effect on the suction side. But they investigated a showerhead with hole spanwise angle of 45°, at an exit Mach number of *Ma* = 1.0.

The mechanisms involved in the interaction of the coolant flow and the mainstream were highlighted by using off-the-wall techniques such as thermal profiles, flow visualizations and

velocity field measurements. Cutbirth and Bogard [11] showed that the cooling jests from the showerhead do not stay attached to the surface, even at relatively low blowing ratios. Moreover, they demonstrated that merging of adjacent coolant jets may occur at high enough *BR*, causing a significant increase in effectiveness levels. This effect was found to be reduced at high mainstream turbulence condition. Nathan et al. [12] confirmed that adiabatic film effectiveness improved continuously with increasing *BR* despite separation of the coolant jets. Polanka et al. [13] commented on a build-up of the coolant along the span of the airfoil to explain the reason why adiabatic effectiveness increased while moving in the direction of coolant hole orientation. Strong spanwise variations in cooling performance were detected also in [12] at the higher *BR* values, due to the accumulation of coolant from the lower holes. Jet interaction in showerhead film cooling is not the only source of its complexity. LDV measurements showed that very high levels of turbulence are generated by the mainstream interaction with the cooling jets [13]. This turbulence is also highly anisotropic. Evidence of elevated turbulence levels caused by showerhead injection was also presented in [14-15].

Results from the experimental investigation of the flow field in the showerhead region made it clear that CFD predictions of leading edge film cooling are extremely challenging. On the one hand, cumulative effect of the coolant along the span of the vane requires large computational domain. On the other hand, the mixing of a film cooling flow with the main stream is an unsteady process, with coherent unsteady features highly dependent on *BR* [16]. There have been relatively few numerical studies of realistic turbine vane with showerhead film cooling. Heidmann et al. [17] chose a film cooled Allied-Signal vane design and assumed periodicity in the spanwise direction on the scale of one pitch of showerhead hole pattern. Steady predictions using the k-ω turbulence model were not validated against measurements. Dyson et al. [18] simulated a periodic section of a showerhead by using the k-ω SST model. Adiabatic effectiveness was overpredicted due to limited jet diffusion. Wu et al. [19] modeled the whole span of a showerhead film cooled vane at high free stream

turbulence and realistic exit Mach number, for a *BR* = 1.5. The RANS based v^2-f turbulence model was selected for predicting the adiabatic wall temperature. On the pressure side, the simulated levels of adiabatic effectiveness were in good agreement with measurements. Conversely, the v^2-f model overpredicted the cooling effectiveness on the suction side.

The key point which comes out of film cooling RANS modeling is that isotropic eddy viscosity turbulence models typically underpredict the lateral spreading of the coolant jet and overpredict the vertical penetration [20]. The eddy viscosity hypothesis has been overcome in different ways. For the lowest *BR* of 0.3, Nemdili et al. [21] obtained quite accurate predictions of the laterally averaged effectiveness in the showerhead region of a symmetric airfoil by using a second order Reynolds Stress model, which solves a transport equation for each stress component. However, the cases at higher *BR* were not satisfactorily captured. Anisotropic corrections were proposed by Li et al. [22] for a better modeling of the Reynold stress and the turbulent scalar-flux on a C3X vane with three rows of film cooling holes. Results from the algebraic anisotropic simulations showed a better agreement with the measured film cooling effectiveness, as compared to Rkε and SST turbulence models. Another strategy to improve showerhead film cooling predictions is to resolve unsteadiness. To the authors' knowledge, there have been no combined experimental and computational studies on the unsteady behavior of showerhead cooling jets in a stator vane. Scale-Resolving Simulations, being computationally intensive, have been applied to representative leading edge models. In 2008, Rozati and Tafti [23, 24] pushed the state of the art in Large Eddy Simulation (LES) by extending it to leading edge film cooling. The model consisted of a cylinder with flat afterbodies. They established that spanwise averaged adiabatic effectiveness is highly sensitive to the coolant inlet flow condition. Moreover, vortex structures playing a role in the mixing of the coolant with mainstream fluid were described in detail, for three *BR* values. Takahashi et al. [25] compared measurements of film cooling effectiveness on a semicircular leading edge model against results from Unsteady RANS and DES based on Spalart-Allmaras turbulence model.

The latter only predicted the ingestion of main flow into film cooling holes. In addition, DES showed good performances in estimation of spanwise averaged η, but with quantitative discrepancies in local peak of effectiveness. Authors suggested that Spalart-Allmaras turbulence model can suffer from lack of unsteady vortex structures in the accelerated flow along the leading edge curvature. However, Funazaki et al. [26] confirmed that discrepancy between η measurements and DES results is evident in the flat plate region of a leading edge model, even when SST is chosen as turbulence model. As far as the DES modeling of leading edge film cooling is concerned, the study by Liang and Kang [27] deserves a mention. They analyzed the influence of positive pressure gradient on unsteadiness within the cooling jet on a rotor cascade. The pressure gradient around the leading edge was found to be responsible for vortex structures break up downstream of the cooling hole.

The object of this work is to experimentally and numerically investigate the effects of blowing conditions on showerhead film cooling performance within a first-stage nozzle guide vane at high mainstream turbulence and realistic Mach number. The measured distributions of adiabatic effectiveness within the showerhead region at different blowing ratios are compared with steady RANS predictions employing commonly used two-equation turbulence models. Moreover, the DES approach is used to clarify the unsteady physics of leading edge film cooling, at an intermediate *BR*. The focus is on coolant jets interaction with the mainstream, under the complexity introduced by flow stagnation, high free stream turbulence, positive pressure gradients and flow acceleration around the pressure and the suction side of the vane. The original contribution of the present study is to validate time-dependent predictions of showerhead film cooling over the whole span of a realistic airfoil geometry. This is indeed a very challenging test to evaluate the DES potential and a chance to better understand the behavior of an hybrid RANS/LES approach, in the presence of jet lift-off and reattachment. Actually, DES is well understood in thin boundary layers, covered by RANS model, and in regions of massive separation, covered by LES model.

EXPERIMENTAL SETUP

Geometry and test conditions

The experimental campaign was carried out at the Energy System and Turbomachinery (EST) Laboratory of Bergamo University, in the context of a National Research Project (PRIN 2010/2011). A continuous running suction type wind tunnel is available to test nozzle vane cascades. The wind tunnel is entirely made up of Plexiglas (thermal conductivity of k = 0.179 W/mK) to assure a complete optical access (Fig. 1). The cascade model consists of a 6 high loaded vanes cascade (Zweifel coefficient of 1.18) whose geometry (Fig. 2) is typical of a first high pressure turbine vane of a modern heavy-duty GT. The vane profile is characterized by a pitch to chord ratio of s/C = 1.04 and an aspect ratio of H/C = 0.69. The flow turning angle at design point is 73.5°. The cascade has been tested at an exit Mach number of Ma_{2is} = 0.42. The inlet turbulence intensity level was increased with respect to the free admission level (1.6%) by installing a grid of cylindrical rods in the wind tunnel inlet section. A 9% Tu_1 level at the vane leading edge plane was obtained by adopting 10 mm diameter rods and adjusting the distance of the grid from the cascade.

Cascade operating conditions (Table 1) were controlled through a continuous monitoring of inlet total and static pressure and exit static pressure (X/C_{ax} = 1.45). Inlet total pressure and static pressure were measured in the admission section by a three-hole probe located at 1.6 C_{ax} upstream of the cascade leading edge. At the same location, inlet boundary layer and turbulence intensity were also measured by means of a flattened Pitot tube and a hot-wire single wire probe (Fig. 3). The numerical integration of the autocorrelation function of the acquired hot-wire signal yielded an integral length scale Λ_x of 11.8 mm.

The leading edge of the three central vanes is equipped with four staggered rows of cylindrical holes (Fig. 2). The stagnation point is located on the showerhead region between the 2nd and the 3rd row of holes, with 2 rows provided on both the pressure side and the suction side of the stagnation point. Each row is composed of 16 cooling holes. Within each row, the hole-to-hole pitch is 5.9D

and the hole length is 2.9*D*. The diameter of the cooling holes *D* is 1.0 mm. Holes are spread over 90% of the vane height. The holes are angled at 45° to the surface. A secondary air supply system was used to feed the cooled vanes. Blowing ratios *BR* up to 4.0 were considered.

Measurement techniques

Profile pressure distribution was measured by an instrumented vane equipped with 39 wall taps, distributed along the vane mid span (δMa_{is} = ± 2 %). Coolant injection conditions were controlled through a continuous monitoring of coolant mass flow and of the corresponding total pressure and temperature. The injected mass flow was measured by an orifice device.

Coolant total pressure and temperature were measured in the feeding chambers inside of the vanes by pressure taps and T-type thermocouples. A maximum variation of ± 0.15% between the three vanes coolant total pressure assured a proper flow sharing between the three cooled vanes. m_c uncertainty was computed according to international standards for orifice devices (EN ISO 5167-2:2003(E)). Based on a 95% confidence interval δm_c resulted to be always lower than ± 2.1%. *BR* values were computed from coolant to mainstream mass flow ratios and the corresponding area ratio.

Film cooling effectiveness distributions on the vane were obtained using the Thermochromic Liquid Crystal technique. Due to the presence of the turbulence generator, a direct access to the leading edge region was not allowed. To overcome this problem, a 6 mm diameter borescope was connected to the camera (Fig. 4). With the aim of capturing the color changes along both pressure and suction side, the borescope was moved tangentially and rotated as well to maintain the view as perpendicular as possible to the surface (Fig. 4). No special problems were detected along the pressure side, where the curvature is quite limited. Conversely, several problems were encountered along the suction side, where curvature effects are stronger. For this reason the TLC were calibrated both on a flat surface and on a cylindrical one, allowing to select the proper calibration curve depending on the surface curvature (Fig. 5). The investigated surfaces are illuminated by means of

two strips of white light LED whereas the color play of TLC is captured by a Nikon D7100 camera through the borescope. All calibrations and measurements were performed in the dark, in order to eliminate any influence of background illumination. Moreover, an illumination intensity as uniform as possible was provided to the model surface by properly orienting the lighting system, in the meanwhile avoiding any light reflection onto the borescope. Viewing and lighting of the vane being inspected by the borescope had constraints in spanwise direction. For this reason, distributions of η were reported from 2.5% to 70% span.

Quasi-steady test was performed to get film cooling effectiveness. Experiments were carried out by heating the coolant, with the mainstream flow at room temperature. During tests, the ambient temperature (about 25°C) was controlled in order to have a red vane surface colour as uniform as possible, i.e. at the lower bound of TLCs active band, with the wind tunnel running at the tested Mach number.

The showerhead cooling supply line was previously set at the desired mass flow rate and cooling air was heated up at about 43°C (resulting in a density ratio *DR* of about 0.95), but blowing in atmosphere. When a stable cooling temperature is reached and the vane surface looks red, the cooling lines are suddenly connected to the vane cavity. In the meantime camera starts acquiring images at a fixed rate of 1 fps; temperature variation inside the vane feeding chambers T_c and main flow temperature T_∞ are acquired as well for a test duration of 60s. RGB to HUE conversion is applied to a single image captured at t = 25s after the start (i.e. when a stable temperature level is reached inside the plenum and on the vane surface). The vane surface temperature measured by TLC in the showerhead region was lowered to eliminate conduction effects in between the rows of holes. That reduction was derived from a preliminary time dependent FEM simulation carried out using COMSOL Multiphysics®. Figure 6 shows the calculated midspan vane surface temperature distribution at t = 25s after the injection and the derived correction curve around the leading edge, at *BR* = 3. The correction was assumed to be constant across the vane span. Therefore conduction

effects are still present around each cooling hole, but to a lesser extent. This procedure resulted in a reduction of the measured temperature by up to 2.2°C, within -0.05 < *s/C* < 0.05. More details on FEM simulation, TLC calibration and data correction for conduction effects can be found in a previous paper by the present authors [28].

Film cooling effectiveness uncertainty depends on TLC and thermocouple measurements and conduction effects. In regions where conduction phenomena do not exist, the η uncertainty will range from ± 4.7 % with η = 0.6, up to about ± 15 % when η = 0.1.

NUMERICAL METHOD

The ANSYS Fluent code was employed to model the leading edge showerhead film cooling in accordance with RANS and scale resolving methods. POINTWISE by Pointwise, Inc was used for grid generation. All computations were carried out on 128 processors at 2.4 GHz, running under LINUX.

Domain and boundary conditions

A side view of the 3D numerical domain is shown in Fig. 7. One full vane passage was represented with periodicity conditions set in the tangential direction to simulate a linear cascade arrangement. The coolant plenum, 64 cooling channels of showerhead type and the vane passage were included in the 3D domain extending over the whole span. The inlet of the passage was located 1.6 C_{ax} upstream of the vane leading edge, where total pressure and turbulence intensity were available from experiments. The outlet was located well downstream (1 C_{ax} downstream of the vane trailing edge).

The boundary conditions prescribed total pressure for the mainstream and static pressure at the outlet (87000 Pa), in order to assure Ma_{2is} of 0.42. The inlet boundary layer taken from the experiments (Fig. 3) was imposed in terms of total pressure profile at the mainstream inlet. An inlet turbulence intensity of Tu_1=13% was set at the inlet of the passage to match the measured Tu_1 levels of 9% at the leading edge plane. The plenum inlet coolant mass flow rate corresponded to the tested

BR values of 2.0, 3.0 and 4.0. Turbulence intensity and length scale of the coolant were computed referring to correlations [29], and varied with *BR*. Both mainstream and coolant flow were assumed to be air whose total temperature was set at $T_{t\infty}$ = 298.5 K and T_{tc} = 323 K, respectively. Air properties were set to be temperature dependent. Here attention is drawn to adiabatic simulations.

Computational mesh

The numerical domain was discretized using an unstructured, multi-block, polyhedral mesh. Prism layers were not used to avoid transition from high aspect ratio hexahedral cells near walls to low aspect ratio cells away from walls, which would endanger convergence. A cross sectional view of the mesh employed in the calculations is shown in Fig. 8. The block surrounding the leading edge over a range of *s/C* = -0.11 on the suction side to *s/C* = 0.26 to the pressure side was used to control the mesh refinement in the showerhead region. Table 2 indicates that the number of cells in the leading edge block is progressively increased up to about 5.6 million in the fine grid. Outside the leading edge block, the mesh was simply extruded in the spanwise direction, with a constant cell size, to obtain the 3D vane passage. This kept the total number of grid cells under 19 million. Local refinement was also provided near and within the cooling holes (Fig. 9).

For the steady simulations, analysis of mesh sensitivity was based on spanwise-averaged film cooling effectiveness values (η_{av}) for the three levels of mesh reported in Table 2. At the lowest *BR* of 2.0, the distributions of η_{av} computed using the medium and fine mesh are almost identical (Fig. 10). Moreover, the medium grid was verified to be sufficient for RANS computations at higher *BR*. Fig. 10 shows that η_{av} deviated by less than 3.4% for medium and fine grids, at *BR* = 3.0.

The predictions in the film-cooled region did not change significantly on further grid refinement even when applying DES. Three monitoring points were located at different spanwise positions, i.e. *z/H* = 0.3, 0.5 and 0.6, to capture the mixing between the mainstream and coolant exiting the showerhead holes (*s/C* = -0.064, -0.016 and 0.068). There are minor differences (< 2.71%) between the time averaged values of temperature at monitor points from medium and fine grids. In order to

ensure accuracy of the unsteady calculations, comparisons of the vane surface temperature contours between DES predictions with medium and fine grids were also carried out, for the same time instant. Medium mesh results showed a small difference from the fine mesh ones. Thus, the medium mesh was adopted for DES modeling. Its size varies in the leading block due to clustering near the injection holes: grid spacing along *x*-streamwise, *y*-wall normal and *z*-spanwise directions are Δx^+ = 17.2-35.1 , Δy^+ = 2.3-4.9 and Δz^+ = 8.2-15.3. Averaged values of the wall shear stress were used to compute the reported Δx^+, Δy^+ and Δz^+. The $y+$ values along the stagnation line are smaller than 2.6. The averaged $y+$ in the showerhead region, within -0.048< s/C <0.059 is 3.4, at BR = 3.

Numerical settings

The 3D Navier-Stokes equations were solved for compressible flow assuming the ideal gas law for the equation of state. The default value of the turbulent Prandtl number (0.85) was retained. For the steady RANS simulations, the SST k-ω turbulence model with Low Reynolds correction and the Realizable k-ε turbulence model with enhanced wall treatment provided closure. Both the models were chosen because of their widespread use in industrial applications of CFD to film cooling. Their validation against experimental thermal fields and effectiveness has already been done for a leading edge model [30]. It turned out that neither the Rke nor the SST can adequately simulate the diffusion of the coolant jet, particularly at the stagnation line. Despite this, predictions of η_{av} with the Rke model were in very good agreement with the measurements, while predictions with the SST model exceeded the observations, on average, by 25%. All equations were discretized with second-order accuracy and residuals were kept under 10^{-6}.

With regard to unsteady modelling, the Realizable k-ε based DES [31] was chosen among hybrid RANS/LES methods. DES switches between RANS and LES models based on the local grid spacing, with wall boundary layers entirely covered by the RANS mode and free shear flow computed in LES mode. Note that the delayed concept to preserve the RANS mode throughout the boundary layer was not applied even though Delayed DES is a recommended practice over DES

[32]. But the shielding function, which provides protection against the grid induced separation, can limit the LES capability of the model [33]. Actually, thin viscous layers, such as those that exist near the stagnation point and the leading edge [34], are suitable for DES modelling in its original version. Seen from another point of view, there is no advantage in using Delayed DES instead of DES to model thin boundary layers flow without separation, since both the models rely on the RANS results in the near wall region [35].

DES modelling was conducted with 40 inner iterations to converge for each time step, so that residuals drop by about 4 orders of magnitude. A time step of Δt = 5e-7s was used to achieve a Courant number of $CFL < 1$ in the leading edge region. Time integration was carried out with the bounded second order implicit scheme. The coupled algorithm solved the momentum and the pressure-based continuity equation together. Further details about numerical settings are available in Table 3. The DES computation, with steady state boundary conditions, run for a start-up time of 2000 time steps. Time-averaged statistics were obtained over 10 through-flow times, based on the average coolant velocity at the exit of the showerhead holes and the hole length (1 through-flow = the time required for the coolant to pass through the hole).

RESULTS AND DISCUSSION

Measurements of the surface effectiveness contours in the showerhead region were compared with steady predictions, for different blowing conditions. Furthermore, the DES application to the case at the intermediate *BR* was discussed to highlight any improvements over the RANS modeling.

Vane loading

Experimental and numerical Ma_{is} profile distributions are shown in Fig. 11 for the solid and the cooled vane, respectively. No load measurements are available for the film cooled airfoil. As expected, the solid and the cooled vane loading (at $BR = 3$) are almost the same, thus showing that predictions compare well with the experimental data. Some minor differences can only be noticed around the showerhead region ($X/C_{ax} < 0.075$), where cooling holes locally influence Ma_{is} values.

The strong acceleration up to about 0.3 C_{ax} along the suction side is due to the blunt leading edge. The Mach number distribution varies smoothly along the pressure side, with progressively increasing flow acceleration up to the trailing edge. The simulation indicates that the stagnation point is slightly shifted to the pressure side. This might be due to the complex interaction between the coolant jets and the approaching head on main flow. Further PIV/LDV measurements are required to verify the stagnation line position with blowing.

Steady predictions vs. measurements of adiabatic effectiveness

Spatial distributions of the measured and simulated effectiveness contours are presented in Fig. 12 for *BR* values of 2.0, 3.0 and 4.0. Measured data collected on the portion of the vane in between the suction side rows were removed since they are affected by excessive levels of uncertainty, due to strong curvature effects. Results from the simulations extend within $-0.11 < s/c < 0.26$, i.e. where the mesh is properly refined (see the dashed rectangle of Fig. 2). Images contain at least 11 holes in a given row, from 2.5% to 70% span.

Spanwise uniformity cannot be established in the measured contours, not even at the lowest *BR*. That is partly due to the fact that coolant is supplied from the hub side. The spanwise motion of the coolant becomes more evident as *BR* increases, leading to progressive accumulation of the coolant toward the tip in the jet exit direction, on both pressure and suction side. Evaluation of the experimental plots suggests that η decays rapidly within a short distance after the stagnation point along the suction side. On the opposite, a better coolant persistence can be obtained along the pressure side, where quite high levels of η can be detected at $s/C = 0.3$. These trends are valid whatever the *BR*.

On the other hand, the direction of the coolant jets (as indicated by the η contour lines of Figs. 12a,d,g) is dependent on *BR*. For the lowest blowing condition, the coolant jets from the pressure side rows have a high enough streamwise component to provide coverage ($\eta > 0.1$) over almost the vane surface at $s/C > 0$, across the whole span. At the higher *BR* of 3.0, the larger spanwise

component of the cooling jets is responsible for improved cooling efficiency (η > 0.35) on the pressure side portion of the vane at *Z/H* > 0.55. A further increase in *BR* to 4.0 enhances the pressure side thermal protection toward the tip due to a more oblique direction of the coolant, but with detrimental effects on film effectiveness in the region within *Z/H* < 0.5, at increasing *s/C*. On the suction side of the vane (*s/C* < 0), adiabatic effectiveness performance is positively affected by increase in *BR*. In fact, higher levels of η can be found downstream of showerhead row #1, at increasing distance from the stagnation line, when comparing Fig. 12a with Fig. 12d. A little increase in adiabatic effectiveness occurs (at *s/C* < 0) as *BR* increases from 3.0 to 4.0. Fig. 12g shows that even at the maximum *BR*, the highest η values on the suction side are located immediately downstream of row#1. A reason for this can be found in the vane loading of Fig.11: strong, favorable pressure gradient around the suction side of the blunt leading edge might help keep coolant jets close to the vane surface.

Extending the analysis to the CFD results, it is evident that there are significant differences between the SST and Rke predictions, and between the simulations and the experiment. However the measured and the computed η levels have the same range in the investigated region of the vane, whatever the *BR*. At *BR* = 2.0, Rke (Fig. 12c) performs better than SST (Fig. 12b) in predicting the surface temperature distribution on the pressure side, especially at *Z/H* > 0.3, where η values are as high as measured and the oblique direction of the coolant traces downstream of row#4 is similar to that in Fig 12a. Both the models predicted lower lateral deflection of the pressure side coolant jets into the spanwise direction at *Z/H* < 0.3. Nevertheless, Figs. 12b and 12c show that the pressure side region of the vane near the hub (*Z/H* < 0.15) is almost uncooled, contrary to what appears in Fig. 12a. This is related to separation of the pressure side cooling jets exiting the holes closer to the hub, for both SST and Rke models (Fig. 13). Actually, those jets are expected to have the largest momentum within each row, since the coolant is supplied from the hub side, but CFD overestimated jet separation and SST predicted even more severe jet lift-off than Rke. Anyway, Fig. 13

demonstrates that pressure side holes suffer from jet separation even at increasing distance from the hub, whatever the turbulence model used. It means that reduction in the jet momentum toward the tip is not enough to prevent separation, even at the lowest *BR*. This is also true for suction side holes. Drawing attention to the vane region at $s/C < -0.05$, Figs. 12b,c report η contours which are different from those measured. The reasons for this are overestimation of the film persistence and underprediction of jet lateral spreading.

At the higher *BR* of 3.0, both the models provided a quite accurate simulation of the film cooling effectiveness on the pressure side, except for the portion near the hub, at $Z/H < 0.2$. The coolant accumulation at increasing *Z/H* is evident from both Figs. 12e,f. The resulting patterns of the η contours are similar to the experiment (Fig. 12d), with Rke yielding the better performance in predicting the oblique travelling of the coolant. Focusing on Fig. 12f, merging of the coolant jets can be noticed just downstream of row#4 at $Z/H > 0.2$, leading to high levels of spanwise uniformity and high effectiveness in the region within $0.06 < s/C < 0.1$. Differences between SST and Rke results are substantial on the suction side. At $s/C < 0$, for the SST simulation (Fig. 12e), distribution of η shows a repeatable periodicity at approximately three pitches with abrupt variation in η values in the region between adjacent holes, due to alternating separation/jet reattachment. The Rke solution (Fig. 12f), which indicates smoother temperature gradient across the span, with progressively increasing η values toward the tip, is closer to the measured thermal field. Unfortunately, the suction side coolant jets extend further downstream before being dispersed, as compared to experiment.

A further increase in *BR* up to 4.0 drastically reduces the accuracy of the simulations, especially on the pressure side. Compared to experimental measurements (Fig. 12g), both the models (Figs 12h,i) computed a wider region of low effectiveness (where $\eta < 0.1$) at $s/C > 0.06$, within $Z/H < 0.4$. This might be due to overprediction of the radial momentum of the separated coolant jets from rows #3 and #4. Moreover, the peak η values which can be detected on the pressure side region

closer to the tip (Z/H > 0.5), downstream of row #4, were underpredicted by both models. Furthermore, the computations missed the pressure side jets trajectory, which becomes more directed in the spanwise direction as *BR* increases. On the suction side, peak η values are well predicted in magnitude and location, especially for the Rke model, but again there is very little lateral spreading of the coolant.

As far as the showerhead region is concerned, the Rke model showed superior performance over SST in predicting effectiveness along the stagnation line and between the pressure side rows, for all *BRs*. Despite weak underestimation of η levels, Rke correctly simulated the measured trend according to which effectiveness within -0.017 < s/C < 0.059 slightly increases with *BR*. At *BR* = 4.0, the Rke pathlines indicate that the cooling jets from row#2 undergo separation, followed by reattachment just upstream of the stagnation line (see black arrows in Fig. 14). Instead, the cooling jets from row #3 separate and partially reattach just upstream of row #4 (see grey arrow in Fig. 14). These two effects help explain why the Rke model computed the highest thermal protection within the showerhead region at the maximum *BR* tested, in agreement with experiments.

For a quantitative assessment of the impact of *BR* on film cooling effectiveness, η values were laterally averaged over the span section shown in Fig. 12 (0.025 < Z/H < 0.7), even though periodicity does not exist. The obtained η_{av} are plotted in Fig 15, at each *BR*. First of all, experiments showed that the η_{av} trend is different for pressure and suction side, depending on main flow acceleration. The measured spanwise averaged effectiveness quickly decreases along the suction side, reaching very low values at s/C = -0.2, whatever the *BR*. The effectiveness trend showing rapid decay within -0.2 < s/C < -0.05 is consistent with [10], where measurements were performed on a showerhead film cooled vane, with the same hole spanwise angle as that assumed here, at high mainstream turbulence.

However, a noticeable improvement in thermal protection is achieved by rising *BR* to 3.0 whereas only a slight increase in η_{av} can be obtained from a further increase in *BR* to 4.0.When

dealing with the vane pressure side, the experimental η_{av} profiles get the peak within a very short distance from row #4 (s/C < 0.12). That maximum η_{av} value, which might depend on merging of adjacent coolant jets, increases with *BR*. Further downstream, η_{av} starts decreasing with increasing s/C due to the strong turbulent dispersion of the coolant jets. The negative and decreasing slopes at s/C > 0.15 are similar for low and medium *BR*. The case at *BR* = 4.0 exhibits the most rapid decrease in η_{av} with increasing s/C, consistently with the results reported in [10]. When evaluating the influence of *BR* on the measured effectiveness around the leading edge (-0.2 < s/C < 0.35), the blowing condition at the medium *BR* resulted in the most effective cooling performance.

It can be deduced from Fig. 15 that the Rke model can predict the η_{av} distribution better than the SST model at low and medium *BR*. At *BR* = 2.0, Rke compared quite well with the experimental data downstream of suction and pressure side rows, even if underprediction of coolant dispersion takes place at s/C > 0.16.

At the higher *BR* of 3.0, Rke still provided reasonable values of η_{av} at s/C > 0.06, whereas η_{av} levels over the suction side are underestimated due to excessive jet separation. As expected, the largest discrepancy between the experimental data and the simulations occurred at the highest *BR*. Both the models computed similar η_{av} values at s/C > 0.8 on the pressure side, but they dramatically underpredicted η_{av} within 0.06 < s/C < 0.2. On the suction side, they suffered again from underprediction of η_{av}, though to a lesser extent for the Rke model.

In addition, the Rke did a better job at predicting the η_{av} profile in the showerhead region, although systematic underprediction occurred for all the investigated BRs. Heat conduction, which affects the region surrounding the cooling holes, may partially explain why the measured η_{av} peaks are higher than those computed, at each row.

DES predictions at *BR* = 3.0

DES was run for the blowing condition of *BR* = 3.0, which assured the highest area-weighted average of effectiveness in the leading edge region. First, the DES capability to resolve the flow

instability in the shear interaction of the coolant with the mainstream was evaluated based on the precursor RANS solution. The ratio of the maximum grid spacing to RANS length scale is below the desired limit of resolution, i.e. $R_l < 0.2$. Secondly, the RANS eddy viscosity μ_t decreased by almost an order of magnitude to accommodate the transition to LES, thus allowing instabilities to develop.

The impact of the scale resolving approach on the coolant jet trajectory is depicted in Fig. 16. Pathlines originating from the showerhead holes showed a chaotic traveling of the coolant in the spanwise direction before turning downstream. The coolant jets exiting rows #2 and #3 can penetrate the mainstream more than they do at rows #1 and #4, because of the low mainstream velocity in the stagnation region. Whatever the row, DES predicted considerable spreading of the pathlines in the wall-normal direction. The graphic evidence of how far into the mainstream the coolant is projected made it clear that jet reattachment is promoted toward the tip, due to a reduced coolant flow momentum. Consequently the accelerating main flow is able to push the coolant streamline down the vane surface, especially on the suction side. Conversely, pathlines are displaced away from the surface near the hub, thus facilitating dilution of the coolant. The intuitive assumption according to which the momentum of the cooling jets decreases toward the tip, since the coolant is supplied from the hub side, was confirmed by Fig. 17. The mass flow rate of the coolant exiting the holes shows a decreasing trend from the hub to the tip, within each row. The holes located close to the sidewalls (holes #1-4 and #13-16) experience the largest change in the outlet flow, whereas the holes located in the central section of the vane discharge comparable amounts of coolant. Holes in row #1 and #2, being located on the suction side, perform better than holes in pressure side rows (#3 and #4). The same conclusion can be drawn looking at values of discharge coefficient C_D presented in Fig. 17b. C_D is defined by the ratio of the actual and the ideal coolant mass flow rate, with the latter resulting from an isentropic expansion from the total pressure in the plenum to the static pressure at the hole exit. For validation purpose, an average of C_D for all the

showerhead holes was computed from the simulations and the experiments, resulting in 0.74 and 0.79, respectively.

The interaction of the coolant with the mainstream was explained by generation of coherent structures. Figure 18 presents the Q isosurface ($Q = S^2 - \Omega^2$ with S being the strain rate and Ω the vorticity), colored by non-dimensional temperature θ. Thus, the blue regions show cooling flow while the red regions are at mainstream condition. The features for each showerhead hole include ring vortices that are formed around the jet and convected downstream. These vortices appear to be of the Hairpin type, rolling up quite regularly from the shear layer between the main flow and the jet core, but they significantly differ from those typically encountered on a film cooled flat plate, as noticed by Liang and Kang [27]. Here, the mainstream pressure gradient plays a fundamental role in determining the shape and the scale of the vortex ring. In fact, along the vane suction side, the Hairpin vortices grow bigger then on the pressure side, due to the higher kinetic energy of the main flow. Moreover, the influence of the mainstream on the vortex ring alignment is evident when looking at the cooling jets from row #1. Jets located near the hub are separated from one another so they cannot resist the bending action by the accelerating main flow. But the spanwise velocity component at the hole exit progressively increases with Z/H. Merging of the coolant jets along row#1 occurred toward the tip, as shown by interaction of the vortex structures from adjacent jets. This causes an increase in cooling performance because the hot gas is prevented from impacting the vane surface. Jets from row #2, being in the near vicinity of the stagnation point, interact with the oncoming head on main flow. The resulting Q isosurface can be explained by tilted vortex rings which quickly destabilize and degenerate into twisted tubular like vortical structures, as they travel both laterally and normal to the surface. As observed in [36], the coolant is transported away from the surface, with unfavorable effect on the film cooling effectiveness around the stagnation line.

On the other hand, jets from pressure side rows are characterized by an almost uniform motion along the span, even though an increase in the spanwise component can be detected at increasing

distance from the hub. In this case, interaction of vortex structures takes place between multiple rows, namely #3 and #4, whereas jets along the same row maintain a distinct path. Further downstream of the hole exit, the ring vortices break up and degenerate into small scale turbulence, whatever the row.

DES time averaged effectiveness contours are shown in Fig. 19 for a comparison against the measured η distribution of Fig. 12d and the steady predictions of Fig. 12f. Once again, as for RANS predictions, the region near the hub is a source of discrepancy between DES results and experimental data, with the former indicating lower η values than measurements at $Z/H < 0.2$. The cause of this is overestimation of separation for the jets #1-3 (those discharging the highest amount of coolant for a given row), and underestimation of their spanwise momentum. As a consequence, the predicted effectiveness iso-contours in the bottom left portion of Fig. 19 are aligned with the streamwise direction, differently from Fig. 12d, where an oblique pattern is evident. Actually, the simulated trajectory of the jets #1-3 may be significantly affected by the assumed inlet condition for the plenum, i.e. uniform velocity coolant flow. With the exception of the portion within $Z/H < 0.2$, the most significant improvement of the DES model over the steady one can be noted on the suction side, where values of η are as high as those measured immediately downstream of row#1, due to the increased mixing. Jet traces, which were evident at $s/C < -0.06$ in the RANS results, cannot be clearly detected in the DES contours of η, by virtue of larger lateral spreading. The deviations between RANS and DES simulations decrease at $s/C > 0$. In fact, both DES and RANS predicted wide variation of η along the span, between the 3rd and the 4th row of holes. Moreover, DES and RANS computed similar oblique patterns of the effectiveness iso-contours downstream of row#4, both showing the most effective coverage near the tip.

For further validation of DES results against experimental data, η was laterally averaged within $0.025 < Z/H < 0.7$, as was done in the previous section for the steady modeling (Fig. 20). DES and RANS predicted almost the same peak η_{av} value on the pressure side, whose magnitude is slightly

underestimated compared to experiments. Furthermore, both the simulation techniques showed a similar η_{av} trend progressing downstream along the pressure side, with a tendency to overestimate η_{av} at $s/C > 0.16$. DES performed better than RANS at $s/C < -0.06$, where unsteady predictions of η_{av} are in very close agreement with the measured data.

Finally, this study provided an opportunity to take stock of DES vs. RANS modelling of leading edge film cooling. Given the much higher computational cost (about 93000 CPUh), the former predicted more realistic η levels on the suction side than the latter. However, the computed amount of decrease in η_{av} along the pressure side is less than measured, even using DES. The reasons for differences between DES and experiments can be found in the so-called “Grey Area”, (i.e. that part of the flow domain where the transition between RANS and LES takes place and, despite being in LES mode, the flow field does not contain enough resolved turbulence). Foroutan and Yavuzkurt [37] pointed out that this error may become severe in film cooling applications, where boundary layer separates from and reattaches to the surface. Another issue deals with perturbed inflow boundary conditions in DES modelling. Further studies are needed to evaluate the influence of imposing synthetic turbulent fluctuations at the mainstream inlet on showerhead film cooling. Moreover, it should be taken into account that velocity profile and turbulence level of the coolant at the inlet plenum can affect the discharge behavior of the cooling holes, especially those located near the hub.

CONCLUSIONS

In this experimental and numerical study, measurements of adiabatic effectiveness for showerhead film cooling within the leading edge region of a first stage vane were used to validate predictions from steady RANS and DES models. The tested conditions prescribed compressible, high turbulent flow for the mainstream and three blowing conditions for the coolant, namely *BR* of 2.0, 3.0 and 4.0, which is discharged through four rows of showerhead holes angled at 45° to the surface.

From the experiments it was clear that: i) the dominant effect for the film effectiveness is the coolant accumulation toward the tip, in the jet exit direction; ii) the coolant persistence is higher along the pressure side of the vane as compared to the suction side, where jet dissipation is enhanced by the mixing with the accelerating mainstream; iii) substantial increase in effectiveness is achieved when *BR* increases from 2.0 to 3.0 whereas detrimental effects on the downstream thermal coverage along the pressure side arise by increasing *BR* to 4.0, due to the assumed injection angle.

Under the RANS approach, the Rke turbulence model was generally better than the SST model at predicting effectiveness, despite some limitations. At low and medium *BR*, Rke performed reasonably well along the pressure side but lateral spreading and mixing were underestimated along the suction side. The mismatch between the Rke results and the measured effectiveness became more severe at the highest *BR*. In this case, the cooling efficiency downstream of the pressure side holes was considerably underestimated, especially near the hub, because of exaggerated jet lift-off.

Focusing on the medium *BR* value of 3.0 (trade-off between cooling air consumption and cooling efficiency), a more accurate simulation of the effectiveness distribution around the leading edge was achieved using the DES model. This is especially true for the suction side of the leading edge, where DES provided an enhancement of mixing between adjacent coolant jets, producing larger degree of spanwise uniformity and higher effectiveness, with respect to the RANS model. Another aspect to be considered is that DES enabled the development of coherent structures in the shear layer between the main flow and the jet core, whose evolution was found to be strongly dependent on the mainstream pressure gradient. Interaction of coolant jets within the same row was prevalent on the suction side of the showerhead whereas merging of jets from different rows occurred on the pressure side.

Further development of this work will consist in comparing DES predictions of the showerhead flow against unsteady PIV and LDV measurements.

ACKNOWLEDGMENTS

The authors gratefully acknowledge the Italian Ministry of Instruction, University and Research (MIUR) for funding this research project (PRIN2010-2011). Moreover, this work has been supported by CINECA Consortium through a ISCRA (Italian SuperComputing Resource Allocation) 2015 grant. Finally, Prof. Perdichizzi is gratefully acknowledged for his support.

NOMENCLATURE

$A_c = N\pi D^2/4$

$A_\infty = 0.9Hs$

$BR = MFR\,A_\infty / A_c$	blowing ratio
C	blade chord
C_D	discharge coefficient
CFL	Courant-Friedrichs-Lewy
D	hole diameter
$DR = \rho_C/\rho_\infty$	density ratio
H	blade height
k	turbulent kinetic energy
Ma	Mach number
$MFR = m_c/m_\infty$	coolant-to-mainstream mass flow ratio
N	number of showerhead holes
$R_l = \Delta_{max}\left(\frac{\varepsilon}{k^{3/2}}\right)_{RANS}$	limit of resolution
$Re_{2is} = U_{2is}c/\nu$	isentropic outlet Reynolds number
s	blade pitch
	curvilinear coordinate
t	time

T	temperature
Tu	turbulence intensity level
X,Y,Z	cascade coordinate system
β	flow angle (axial direction)
Δ	grid spacing
ε	turbulent dissipation rate
Λ_x	length scale
$\eta = (T_{aw} - T_\infty)/(T_c - T_\infty)$	film cooling effectiveness
$\theta = (T_{gas} - T_\infty)/(T_c - T_\infty)$	normalized temperature
ν	kinematic viscosity
μ_t	kinematic turbulent eddy viscosity
ρ	flow density

Subscripts

1	inlet
2	exit
av	laterally averaged
ax	axial
aw	adiabatic wall
c	cooling flow
is	isentropic condition
t	total
w	wall
∞	free stream

REFERENCES

[1] Dick, E., 2015, “Fundamentals of Turbomachines”, Springer, ISSN 0926-5112.

[2] Cunha, F. J., 2006, “Heat Transfer Analysis”, chapter 4.4, The gas turbine handbook, NETL.

[3] Bogard, D. G., 2006, “Airfoil Film Cooling”, chapter 4.2.2.1, The gas turbine handbook, NETL, 2006.

[4] Wadia, A. R., and Nealy, D. A., 1985, “Development of a Design Model for Airfoil Leading Edge Film Cooling”, ASME Paper No. 85-GT-120.

[5] Reiss, H., and Bolcs, A., 2000, “Experimental Study of Showerhead Cooling on a Cylinder Comparing Several Configurations using Cylindrical and Shaped Holes”, ASME J. Turbomach. 122(1), pp. 161-169.

[6] Cruse, M. W., Yuki, U. M., and Bogard, D. G, 1997, “Investigation of various Parametric Influences on Leading Edge Film Cooling”, ASME Paper No. 97-GT-296.

[7] Albert, J. A., Bogard, D. G., and Cunha, F., 2004, “Adiabatic and Overall Effectiveness for a Film Cooled Blade”, ASME Paper No. GT2004-53998.

[8] Polanka, M. D., Witteveld, V. C., and Bogard, D. G., 1999, “Film Cooling Effectiveness in the Showerhead Region of a Gas Turbine Vane Part I: Stagnation Region and near Pressure Side”, ASME Paper No. 99-GT-48.

[9] Witteveld, V. C., Polanka, M. D., and Bogard, D. G., 1999, “Film Cooling Effectiveness in the Showerhead Region of a Gas Turbine Vane Part II: Stagnation Region and near Suction Side”, ASME Paper No. 99-GT-49.

[10] Nasir, S., Bolchoz, T., Fai Ng, W., Zhang, L. J., Moon, H. K., Anthony, R. J., 2012, “Showerhead Film Cooling Performance of a Turbine Vane at High Freestream Turbulence in a Transonic Cascade”, ASME J. Turbomach. 134(5), p. 051021.

[11] Cutbirth, J. M. and Bogard, D. G., 2002, “Thermal Field and Flow Visualization within the Stagnation Region of a Film Cooled Turbine Vane”, ASME J. Turbomach. 124(2), pp. 200-206.

[12] Nathan, M. L., Dyson, T. E., Bogard, D. G., Bradshaw, S. D., 2013, “Adiabatic and Overall Effectiveness for the Showerhead Film Cooling of a Turbine Vane”, ASME J. Turbomach. 136(3), p. 031005.

[13] Polanka, M. D., Cutbirth, J. M., and Bogard, D. G., 2002, “Three Component Velocity Field Measurements in the Stagnation Region of a Film Cooled Turbine Vane”, ASME J. Turbomach. 124(3), pp. 445-452.

[14] Cutbirth, J. M., and Bogard, D.G., 2002, “Evaluation of Pressure Side Film Cooling with Flow and Thermal Field Measurements – Part I: Showerhead Effects”, ASME J. Turbomach. 124(4), pp. 670-677.

[15] Cutbirth, J. M., and Bogard, D. G., 2002, “Evaluation of Pressure Side Film Cooling with Flow and Thermal Field Measurements – Part II: Turbulence Effects”, ASME J. Turbomach. 124(4), pp. 678-685.

[16] Fawcett, R. J, Wheeler, A. P. S., He, L., Taylor, R., 2012, “Experimental Investigation Into Unsteady Effects on Film Cooling”, ASME J. Turbomach. 134(2), p. 021015.

[17] Heidmann, J. D., Rigby, D. L., and Ameri, A. A., 1999, “A Three-dimensional Coupled Internal/External Simulation of a Film-cooled Turbine Vane”, ASME J. Turbomach. 122(2), pp. 348-359.

[18] Dyson, T. E., Bogard, D. G., and Bradshaw, S. D., 2012, “Evaluation of CFD Simulations of Film Cooling Performance in the Showerhead Region of a Turbine Vane including Conjugate Effects”, Proc. of IMECE2012, November 9-15, Texas, USA.

[19] Wu, H., Nasir, S., Ng, W. F., Moon, H. K., 2008, “Showerhead Film Cooling Performance of a Transonic Turbine Vane at High Freestream Turbulence (Tu = 16%): 3-D CFD and Comparison with Experiment”, Proc. of IMECE2008, October 31-November 6, Boston, USA.

[20] Acharya, S., Tyagi, M., and Hoda, A., 2001, “Flow and Heat Transfer Predictions for Film Cooling, Heat Transfer in Gas Turbine Systems”, Annals of the New York Academy of Sciences, 934, pp. 110-125.

[21] Nemdili, F., Azzi, A., Theodoridis, G., Jubran, B. A., 2008, “Reynolds Stress Transport Modeling of Film Cooling at the Leading Edge of a Symmetrical Turbine Blade Model”, Heat Transfer Engineering 29(11), pp. 950-960.

[22] Li, X., Ren, J., and Jiang, H., 2014, “Film Cooling Modeling of Turbine Blades Using Algebraic Anisotropic Turbulence Models”, ASME J. Turbomach, 136(11), p. 111006.

[23] Rozati, A., and Tafti, D. K., 2008, “Large-Eddy Simulations of Leading Edge Film Cooling: Analysis of Flow Structures, Effectiveness and Heat Transfer”, Int J Heat Fluid Flow, 29(1), pp. 1-17.

[24] Rozati, A., and Tafti, D. K., 2008, “Effect of Coolant-Mainstream Blowing Ratio on Leading Edge Film Cooling Flow and Heat Transfer - LES investigation”, Int J Heat Fluid Flow, 29(4), pp. 857-873.

[25] Takahashi, T., Funazaki, K., Salleh, H. B., Sakai, E., Watanabe, K., 2011, “Assessment of URANS and DES for Predictions of Leading Edge Film Cooling”, ASME J. Turbomach, 134(3), p. 031008.

[26] Funazaki, K, Kawabata, H., Takahashi, D., Okita, Y., 2012, “Experimental and Numerical Studies on Leading Edge Film Cooling Performance: Effects of Hole Exit Shape and Freestream Turbulence”, ASME Paper No. GT2012-68217.

[27] Liang, J. Y., and Kang, S., 2012, “Investigation of Film Cooling on the Leading Edge of Turbine Blade based on Detached Eddy Simulation”, Science China Technological Sciences, 55(8), pp. 2191-2198.

[28] Barigozzi, G., and Ravelli, S., 2015, “Combined Experimental and Numerical Study of Showerhead Film Cooling in a Linear Nozzle Vane Cascade”, ASME paper No. GT2015-42397.

[29] ANSYS FLUENT 12 user guide, 2009, ANSYS Inc., Canonsburg, PA.

[30] Mathew, S., Ravelli, S., and Bogard, D. G., 2012, “Evaluation of CFD Predictions using Thermal Field Measurements on a Simulated Film Cooled Turbine Blade Leading Edge”, ASME J. Turbomach., 135(1), p. 011021.

[31] Spalart, P. R., Jou, W-H, Strelets, M., Allmaras, S.R, 1997, “Comments on the Feasibility of LES for Wings, and on a Hybrid RANS/LES Approach, Advances in DNS/LES”, Proc. of 1st AFOSR Int. Conf. On DNS/LES, Louisiana, USA.

[32] Menter, F. R., 2012, “Best Practice: Scale-Resolving Simulations in ANSYS CFD”, Version 1.0, ANSYS Report.

[33] Menter, F. R., Schütze, J., Kurbatskii, K. A., Gritskevich, M. S., Garbaruk, A., 2011, “Scale-resolving Simulation Techniques in Industrial CFD”, Proc. of 6th AIAA Theoretical Fluid Mechanics Conference, Honolulu, Hawaii, AIAA 2011-3474.

[34] Jansohn, P., 2013, “Modern Gas Turbine Systems”, Woodhead Publishing, Philadelphia, USA.

[35] Durrani, N., and Qin, N., 2011, “Comparison of RANS, DES and DDES results for ONERA M-6 Wing at Transonic Flow Speed using an in-house Parallel Code”, Proc. of 49th AIAA Aerospace Sciences Meeting, Orlando, Florida, AIAA 2011-190.

[36] Sreedharan, S. S., and Tafti, D. K., 2008, “Large Eddy Simulations of a Three-row Leading Edge Film Cooling Geometry”, Proc. of IMECE2008, October 31-November 6, Boston, USA.

[37] Foroutan, H., and Yavuzkurt, S., 2015, “Numerical Simulations of the Near-Field Region of Film Cooling Jets Under High Free Stream Turbulence: Application of RANS and Hybrid URANS/Large Eddy Simulation Models”, ASME J. Heat Transfer 137(1), p. 011701.

C = 142.1 mm	Ma_1 = 0.12
s/C =1.04	β_2 = 20°
H/C= 0.69	Ma_{2is} = 0.42
β_1 = 90°	Re_{2is} = 1.19 10^6
Tu_1 = 9.0 %	BR = 2.0 - 4.0

Table 1. Cascade geometry and operating conditions.

Grid refinement	**Coarse**	**Medium**	**Fine**
Polyhedra (million)	17.68	18.48	18.76
Million cells in the LE block	4.70	5.31	5.59

Table 2. Grid refinement**.**

Solver	Pressure-based - compressible flow
Momentum **Energy & Density** **Turbulence** **Gradient**	Bounded Central Differencing 3rd order MUSCL 3rd order MUSCL least square cell based

Table 3. Numerical settings for DES computation.

Fig. 1. The wind tunnel.

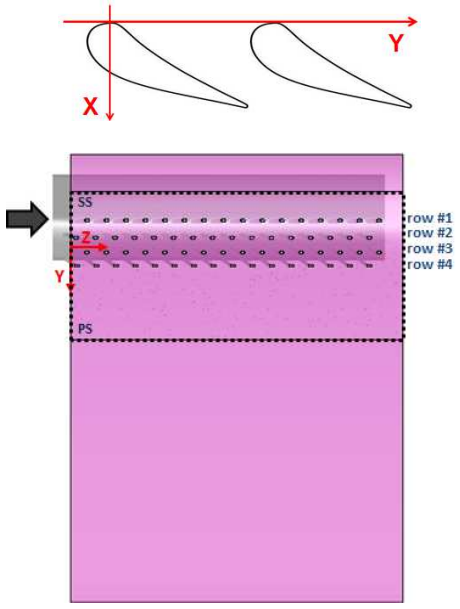

Fig. 2. Cascade model and cooling scheme.

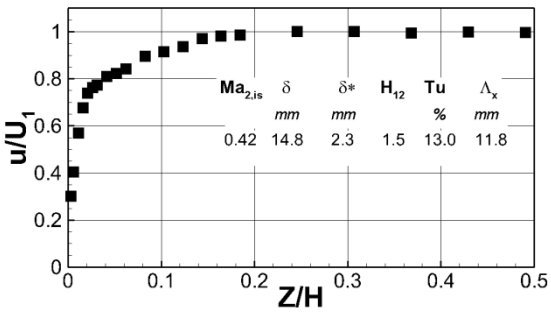

Fig. 3. Inlet boundary layer (X/c_{ax} = -1.6).

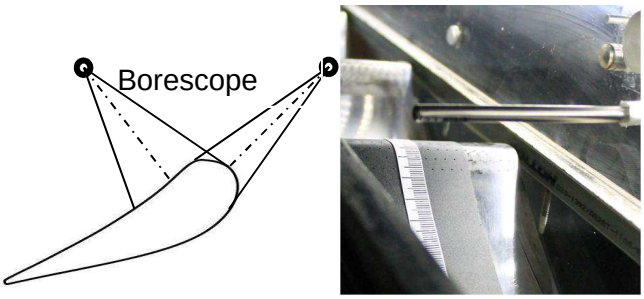

Fig. 4. TLC measurement setup.

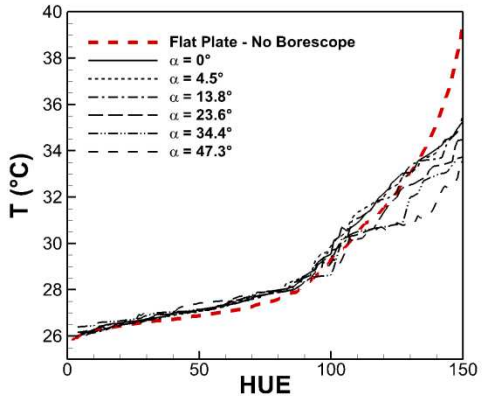

Fig. 5. TLC calibration.

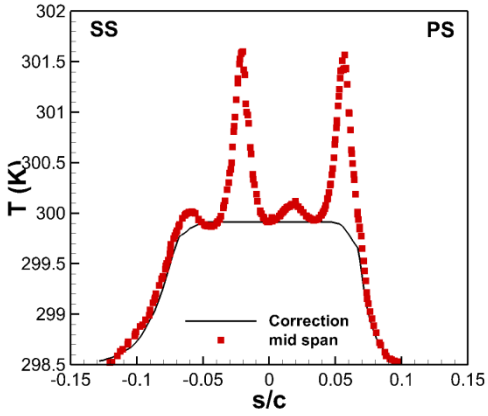

Fig. 6. Conduction correction at time t = 25s.

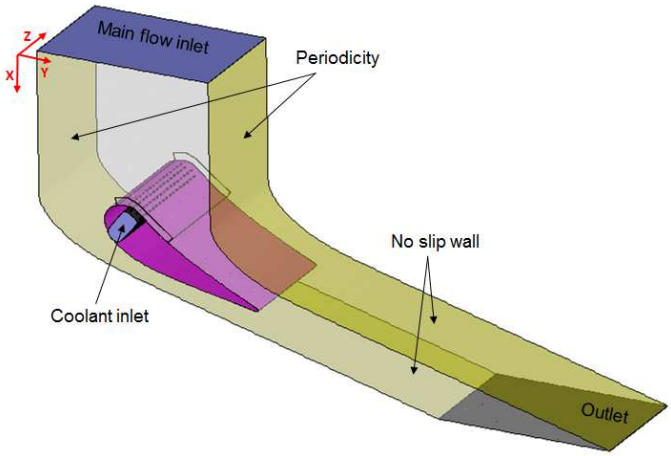

Fig. 7. 3D computational domain and boundary conditions.

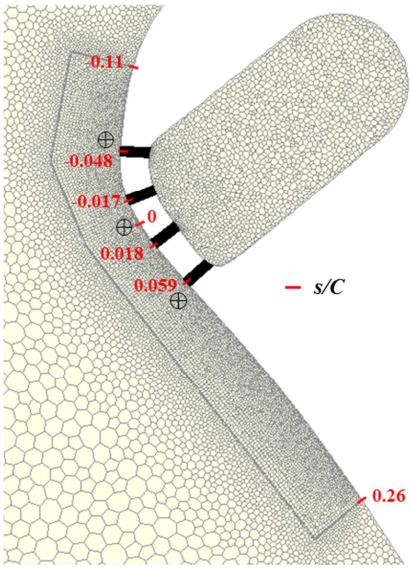

Fig. 8. Cross sectional view of the mesh in the leading edge region with monitor points.

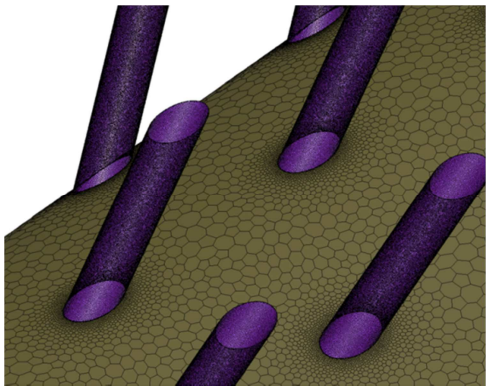

Fig. 9. Zoomed-in view of plenum and cooling holes surface mesh.

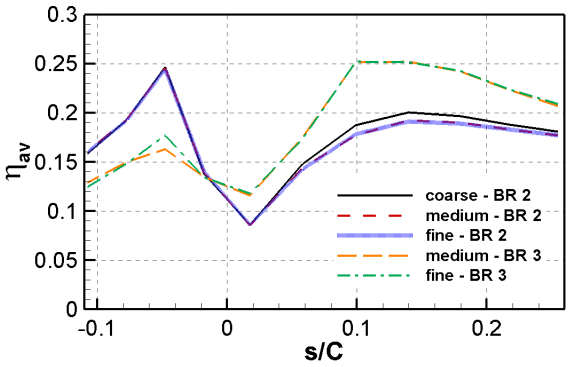

Fig. 10. Grid resolution test at *BR* values of 2.0 and 3.0: SST-RANS predictions of laterally averaged adiabatic effectiveness.

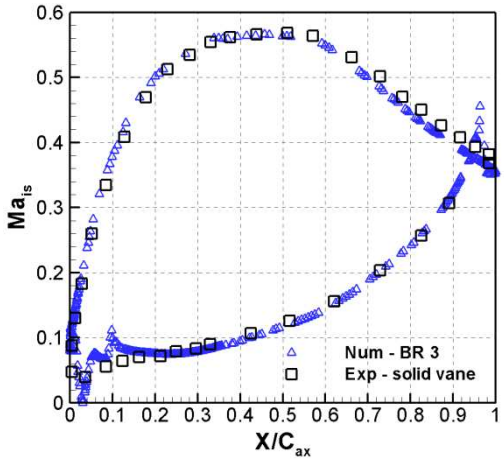

Fig. 11. Ma_{is} distributions for the solid (Exp) and the cooled (Num) vane, at *BR* = 3.0.

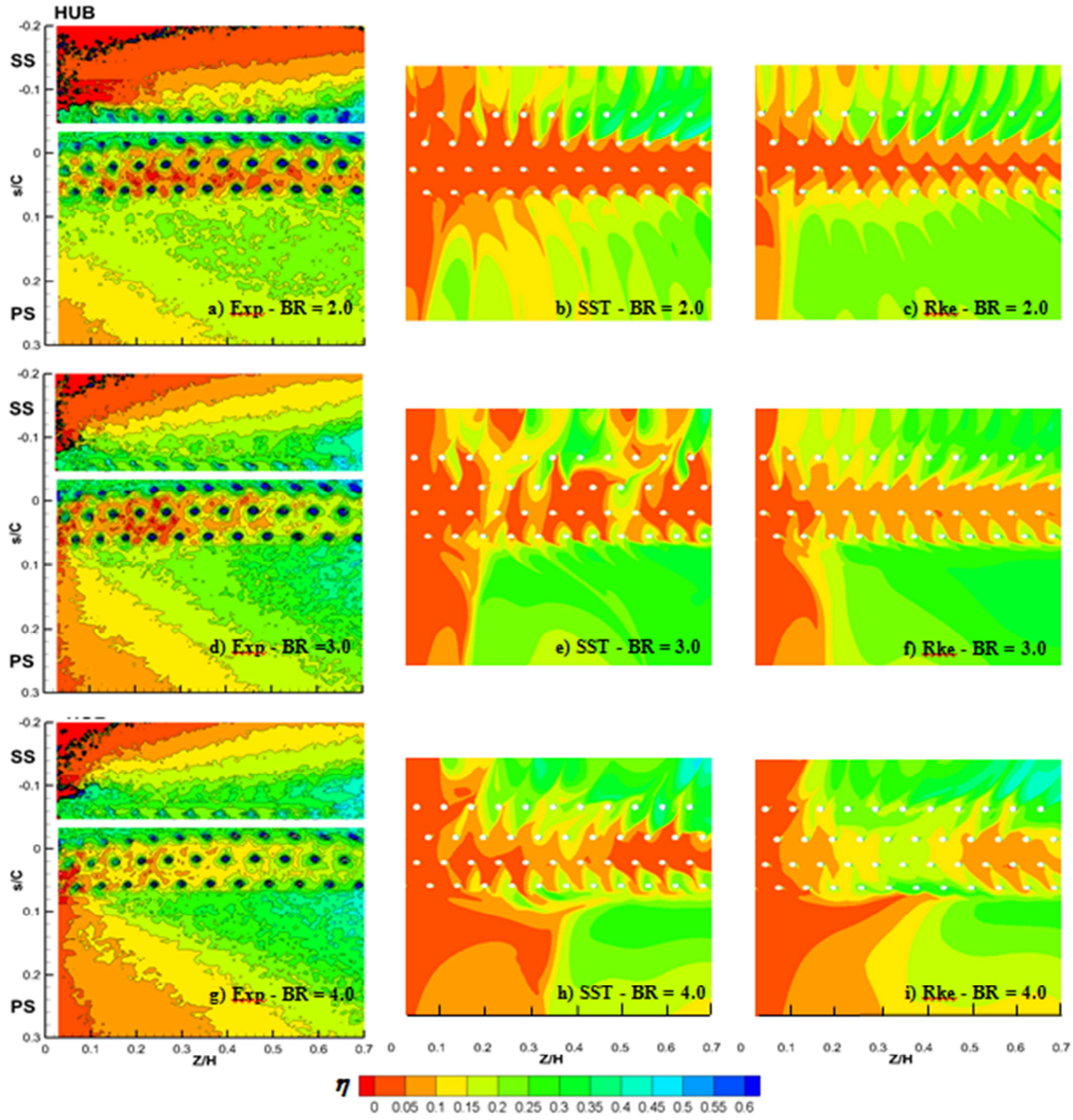

Fig. 12. Contours of adiabatic effectiveness η from experimental measurements (left), SST (middle) and Rke (right) predictions for a-c) BR = 2.0, d-f) BR = 3.0 and g-i) BR = 4.0.

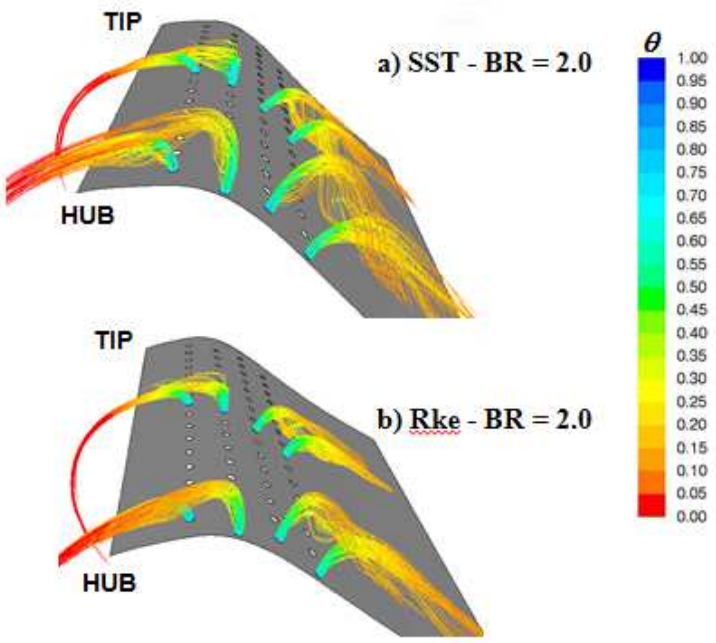

Fig. 13. Pathlines originated from the cooling holes coloured by the normalized temperature θ at BR = 2.0 for a) SST and b) Rke models.

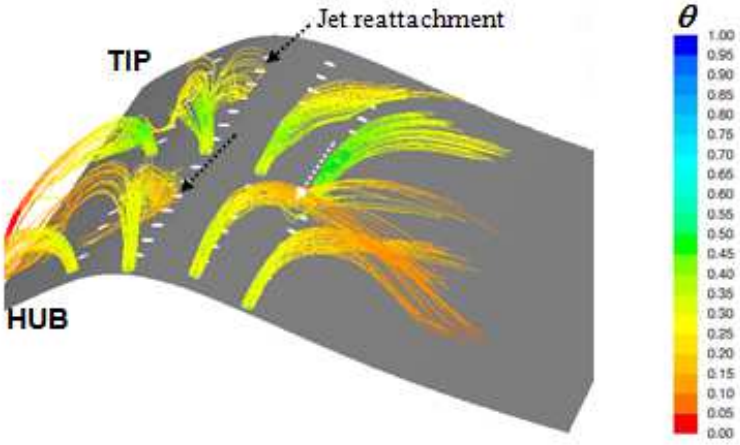

Fig. 14. Pathlines originated from the cooling holes coloured by the normalized temperature θ at BR = 4.0 for the Rke model.

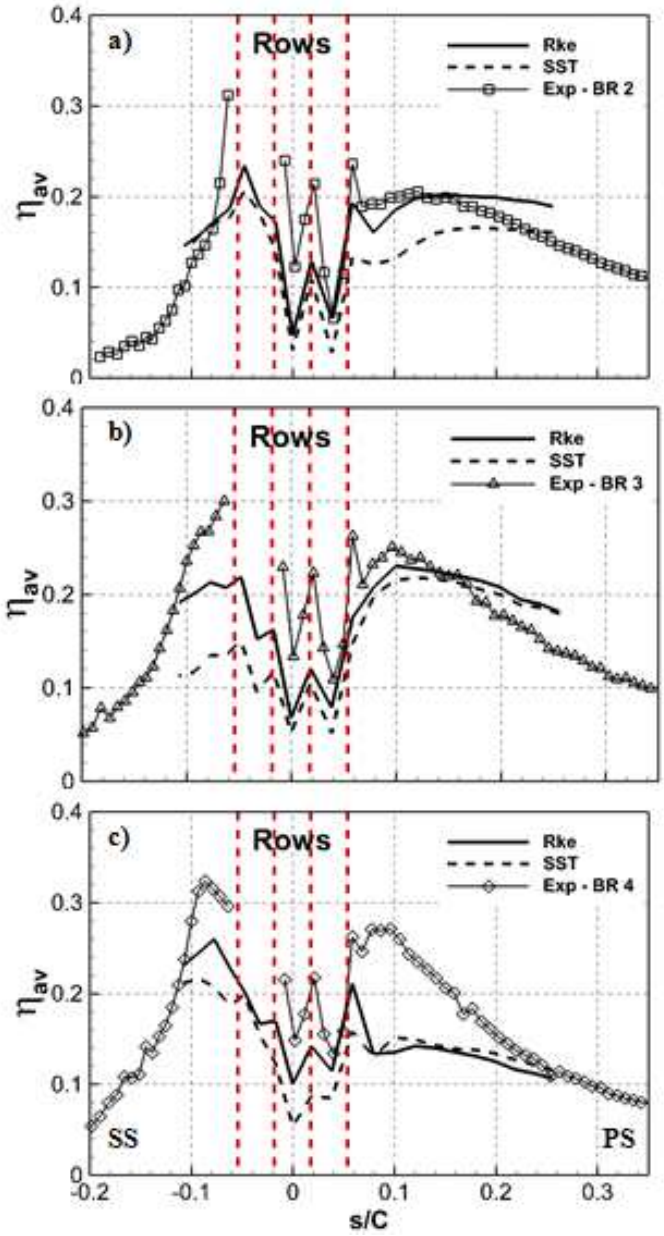

Fig. 15. Measurements (Exp) vs. SST and Rke predictions of laterally averaged adiabatic effectiveness η_{av} at a) BR = 2.0, b) BR = 3.0 and c) BR = 4.0, within 0.025 < Z/H < 0.7.

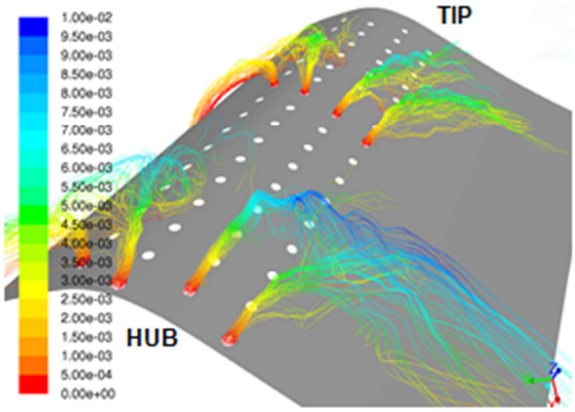

Fig. 16. Instantaneous pathlines originated from the cooling holes coloured by cell wall distance (m) at BR = 3.0, for the DES model.

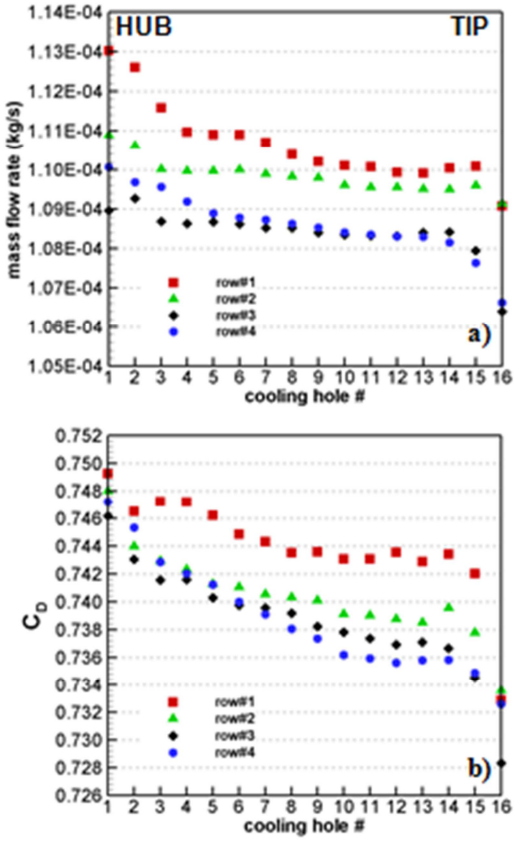

Fig. 17. Predictions of a) outlet coolant flow rate and b) discharge coefficient C_D for the showerhead holes, at BR = 3.

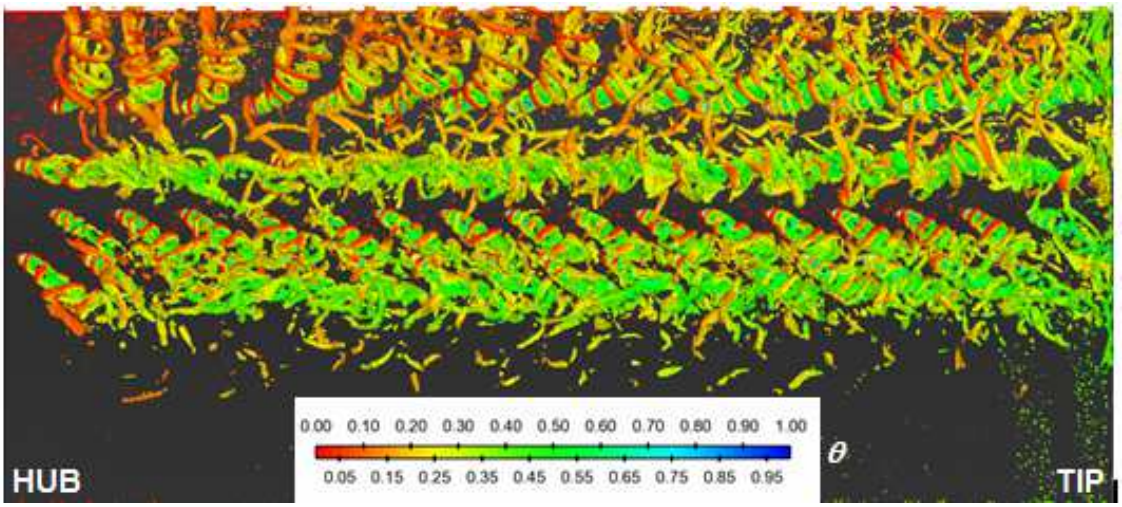

Fig. 18. DES isosurface of $Q = 2*10^9$ s^{-2} coloured by the normalized temperature θ at BR = 3.0 (top view of the showerhead).

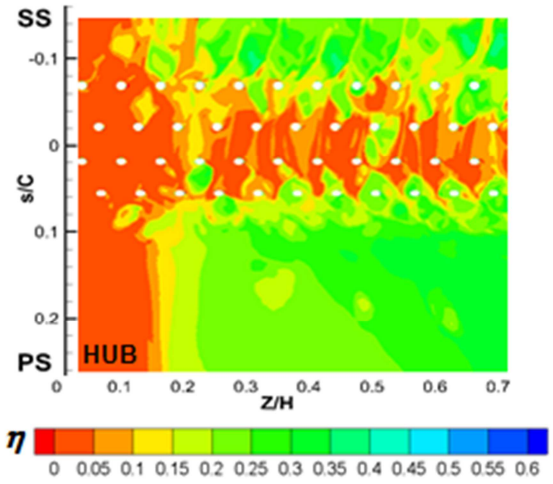

Fig. 19. Time averaged DES contours of adiabatic effectiveness η at $BR = 3.0$.

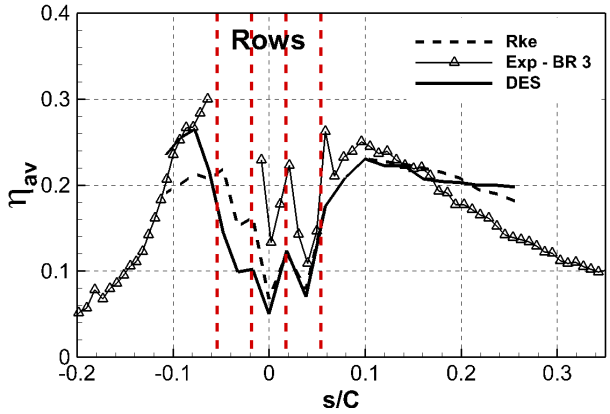

Fig. 20. Measurements (Exp) vs. DES and RANS (Rke) predictions of laterally averaged adiabatic effectiveness η_{av} at $BR = 3.0$, within $0.025 < Z/H < 0.7$.